Kinetics governing phase separation of nanostructured Sn_xGe_{1-x} alloys

Regina Ragan,[1,*] Jonathan E. Guyer,[2] Erik Meserole,[3] Mark S. Goorsky,[3] and Harry A. Atwater[4]
[1]*Department of Chemical Engineering and Materials Science, University of California, Irvine, Irvine, California 92697, USA*
[2]*Metallurgy Division, National Institute of Standards and Technology, Gaithersburg, Maryland 20899, USA*
[3]*Department of Materials Science and Engineering, University of California, Los Angeles, Los Angeles, California 90095, USA*
[4]*Thomas J. Watson Laboratory of Applied Physics, California Institute of Technology, Mail Stop 128-95, Pasadena, California 91125, USA*
(Received 22 July 2005; revised manuscript received 15 March 2006; published 5 June 2006)

We have studied the dynamic phenomenon of Sn_xGe_{1-x}/Ge phase separation during deposition by molecular beam epitaxy on Ge(001) substrates. Phase separation leads to the formation of direct band gap semiconductor nanowire arrays embedded in Ge oriented along the [001] growth direction. The effect of strain and composition on the periodicity were decoupled by growth on Ge(001) and partially relaxed Si_yGe_{1-y}/Ge(001) virtual substrates. The experimental results are compared with three linear instability models of strained film growth and find good agreement with only one of the models for phase separation during dynamic growth.

DOI: 10.1103/PhysRevB.73.235303 PACS number(s): 68.37.−d, 61.46.−w, 81.07.−b, 81.10.−h

I. INTRODUCTION

Nanostructured materials, such as one-dimensional systems[1] and superlattice structures,[2] are expected to have better performance as thermoelectric coolers in comparison with their bulk counterparts. Theoretical calculations predict an increase in the dimensionless figure of merit, ZT, of thermoelectric coolers for one-dimensional systems. ZT is the product of the electrical conductivity, the temperature, and the square of the Seebeck coefficient, divided by the thermal conductivity. In one-dimensional systems, there is a higher density of states (DOS) at the Fermi level that increases electrical conductivity and phonon scattering at material interfaces reduces lattice thermal conductivity. Both these effects lead to an increase in thermoelectric device performance for nanowire arrays embedded in a matrix. Decreasing nanowire radii using lithographic techniques to reach the size regime where the DOS is altered from bulk properties often has a high price tag and/or low throughput. Using self-assembly to fabricate nanostructures has the advantage of small feature sizes without exotic and expensive lithographic techniques. Phase separation during epitaxial growth is one self-assembly mechanism that produces ordered arrays of nanowires parallel to the substrate normal in the absence of lithography.[3,4] Sn_xGe_{1-x}/Ge films grown on Ge(001) substrates phase separate during deposition and forms nanowire arrays oriented along the [001] growth direction.[3] Our interest in Sn_xGe_{1-x} nanowire arrays was further motivated by the compatibility of this direct band gap group IV semiconductor[5,6] with Si integrated circuits. The Sn_xGe_{1-x} alloy system is a promising material for thermoelectric cooling devices because of the ability to epitaxially grow single crystal Sn_xGe_{1-x} nanowire arrays nonlithographically at a low substrate temperature, $T<453$ K, on Ge/Si(001) substrates.[6] Sn_xGe_{1-x} alloy nanostructured thermoelectric cooling devices may have applications to dissipate heat at local hot spots that limit device performance in Si microelectronic devices.

Previously we have fabricated Sn_xGe_{1-x} nanowire arrays on Ge(001) substrates without lithography.[3] We have also measured how the optical properties vary with microstructure for thin homogeneous Sn_xGe_{1-x} alloy films,[6] Sn_xGe_{1-x} nanowire arrays embedded in Ge,[3] to Sn-rich quantum dots in a Ge matrix.[7] In order to maximize thermoelectric device performance, one must be able to engineer the diameter of the nanowire and the periodicity of the arrays. Therefore, in this paper, the Sn_xGe_{1-x} alloy system was studied both experimentally and theoretically to gain insight into the physical mechanisms driving phase separation and ordering during dynamic growth. Three kinetic models predicting the periodicity of phase separation—referred to as the growth instability wavelength—were compared to the experimentally measured growth instability wavelength. The remainder of the paper will be organized as follows: (Sec. II) Sn_xGe_{1-x} alloy growth, (Sec. III) structural characterization, (Sec. IV) statistical analysis of the periodicity of the growth instability, and (Sec. V) correlation of experiment with the physical models.

II. Sn_xGe_{1-x} ALLOY GROWTH

Sn_xGe_{1-x} alloys were grown by molecular beam epitaxy (MBE) on Ge(001) and partially relaxed Si_yGe_{1-y} films on Ge(001) substrates. Both Si and Ge were evaporated from a copper crucible with an electron beam evaporator and Sn was evaporated with a Knudsen cell. The relaxed Si_yGe_{1-y} films were grown by MBE on Ge(001) substrates with varying Si composition at 873 K with a grading rate of 10% μm to minimize dislocation density.[8] Prior to Sn_xGe_{1-x} growth, the sample was cooled to 433 K to eliminate Sn surface segregation. The Sn_xGe_{1-x} and Si_yGe_{1-y} films were grown at a fixed growth rate, 0.05 nm/s, and 0.15 nm/s, respectively. The crystal surface periodicity and roughness was monitored *in situ* with reflection high energy electron diffraction. Growth of Sn_xGe_{1-x} alloy films on Si_yGe_{1-y}/Ge(001) allowed us to tune the effective lattice parameter of the "virtual" substrate and thereby the strain state of the Sn_xGe_{1-x} films without varying the Sn composition. By varying the effective lattice parameter of the substrate, the dependence on strain and composition of the growth instability was

decoupled.[9] A series of films having a constant Sn composition but differing values of misfit with respect to the virtual Si_yGe_{1-y} substrates were grown. The misfit was varied from 0 to 1%. Alternatively, in order to probe the effect of composition on the growth instability, Sn_xGe_{1-x} films with the misfit engineered to remain constant were grown in the composition range of $0<x<0.035$ for a misfit of approximately 0.5% and in the composition range of $0<x<0.07$ for a misfit of approximately 1%.

III. STRUCTURAL CHARACTERIZATION

The Sn_xGe_{1-x} films were characterized with Rutherford backscattering spectroscopy (RBS), high-resolution x-ray diffraction (HR-XRD), transmission electron microscopy (TEM), scanning TEM (STEM), and atomic force microscopy (AFM). RBS measured the average Sn composition in the Sn_xGe_{1-x} films and the Si composition in the Si_yGe_{1-y} films. HR-XRD measured the strain state of both the Sn_xGe_{1-x} and Si_yGe_{1-y} films with respect to Ge(001), TEM characterized the crystal structure, and STEM analysis in planar view revealed the phase separation of Sn in a rodlike morphology. A height modulation on the surface, corresponding to the phase separation, or growth instability, was measured with AFM for a variety of samples with varying misfit strain and Sn composition. The power spectral density calculated from AFM topological images yielded a value for the fastest growing wavelength of the growth instability.

A. Determination of alloy composition and strain state

RBS measures composition as a function of depth; thus we used RBS to measure the Sn composition profile in the Sn_xGe_{1-x} films and the Si composition profile in the Si_yGe_{1-y} films. The backscattered signal was measured with the samples tilted 7° to the incident 2 MeV He^{++} beam to avoid channeling. RBS resolves compositional variations along the depth profile of the film at nanometer length scales. Analysis of the peak height yields the average Sn composition and the height uniformity demonstrates the uniformity of the Sn composition along the depth profile.[6] At substrate temperatures above $T=473$ K, Sn surface segregation has been observed due to a lower surface free energy of Sn versus Ge.[10] The spot size of the He^{++} beam was on the order of 1 mm and this defines the spatial composition resolution in the plane of the film. The phase-separated regions in the Sn_xGe_{1-x} films are on a much smaller length scale, on the order of 10 nm. Thus the *average* Sn composition in the Sn_xGe_{1-x} alloy film was determined from RBS. In this paper, x will denote the *average* Sn composition in Sn_xGe_{1-x} alloy films.

HR-XRD measured the strain state of both the Sn_xGe_{1-x} alloy film and the Si_yGe_{1-y} virtual substrate. Reciprocal space lattice maps of the (004) and (224) reflections of a Sn_xGe_{1-x} alloy film with $x=0.018$ and $y=0.05$, are shown in Fig. 1(a) and 1(b), respectively. In Fig. 1(a), the (004) reflection of the $Si_{0.06}Ge_{0.94}$ layer is shifted to higher values of a reciprocal lattice vector and that of the $SnGe_{1-x}$layer was shifted to lower values of a reciprocal lattice vector with respect to the surface plane of the Ge(001) substrate. In Fig. 1(b), the (224) reflection combined with the measured reciprocal lattice vector for (004) planes of Fig. 1(a) yields information regarding the state of relaxation of the epitaxial films. The lines are guides to the eye. If the $Si_{0.06}Ge_{0.94}$ peak fell on the vertical dashed line through the Ge(001) substrate peak the $Si_{0.06}Ge_{0.94}$ layer would be fully strained (that is each film has the same in-plane lattice parameter). The intersection of the solid diagonal line and the solid vertical line represents the axis along which the $Si_{0.06}Ge_{0.94}$ peak would

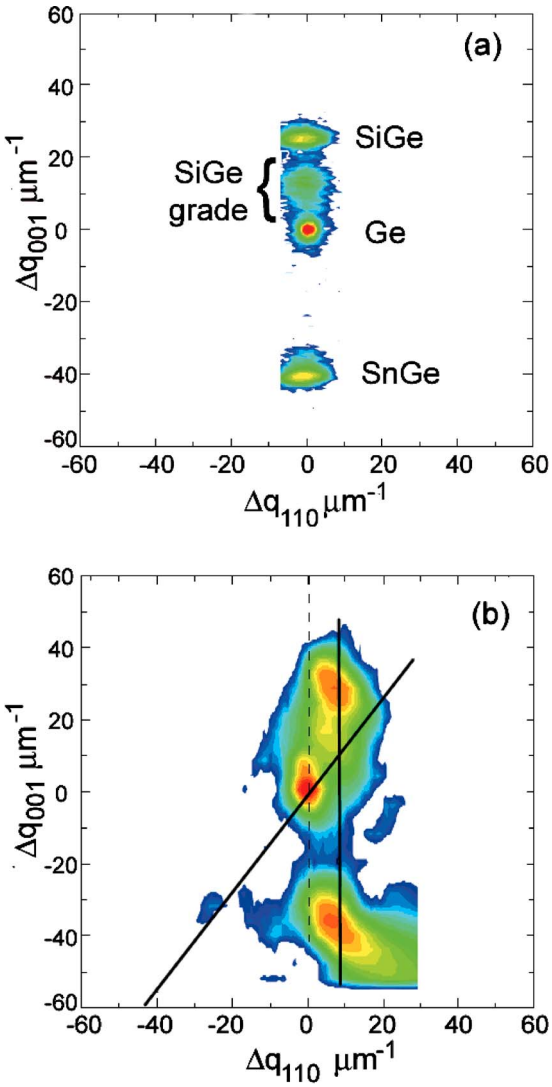

FIG. 1. (Color online) HR-XRD reciprocal lattice maps of $Sn_{0.018}Ge_{0.982}/Si_{0.06}Ge_{0.94}/Ge(001)$ taken with the (a) 004 reflection and (b) 224 reflection. The 004 reflection demonstrates that the $Si_{0.06}Ge_{0.94}$ layer is in tension and the $Sn_{0.018}Ge_{0.982}$ layer is in compression with respect to the Ge(001) substrate. The dashed vertical line in (b) represents a fully coherent film and the solid diagonal line represents a fully relaxed film with respect to the Ge(001) substrate. The vertical solid line represents a fully coherent interface between the $Sn_{0.018}Ge_{0.982}$ and the $Si_{0.06}Ge_{0.94}$ layers. The $Sn_{0.018}Ge_{0.982}$ alloy shows some relaxation, ≈5%, with respect to the $Si_{0.06}Ge_{0.94}$ layer while the $Si_{0.06}Ge_{0.94}$ alloy is 81% relaxed with respect to the Ge(001) substrate.

fall if the layers were fully relaxed. The Si_yGe_{1-y} alloy film is 81% relaxed with respect to the Ge(001) substrate. Another feature evident in the spectra is the Sn_xGe_{1-x} alloy peak is just slightly off the vertical line that intersects the Si_yGe_{1-y} alloy peak, where again intersection with the vertical line would indicate that the films are fully coherent. The Sn_xGe_{1-x} alloy layer was calculated to have very little relaxation, $\approx 5\%$ with respect to the Si_yGe_{1-y}/Ge(001) virtual substrate. By sampling Si_yGe_{1-y}/Ge(001) virtual substrates with varying Si content ($0<y<0.24$) we found that the percentage of relaxation decreased with increasing Si composition. From this we were able to extrapolate the strain state of all the Si_yGe_{1-y} films.

B. Microstructure

Sn_xGe_{1-x}/Ge(001) films with Sn composition of $0<x<0.07$ and film thickness between 0.1 μm and 1 μm were examined in TEM and STEM. Previously, solid solutions of 100 nm thick Sn_xGe_{1-x} films with Sn compositions between $0<x<0.115$ were grown and characterized to be coherent with the Ge(001) substrates.[6] Here we first compare the microstructure observed in TEM as a function of film thickness. A 100 nm $Sn_{0.06}Ge_{0.94}$/Ge(001) film was analyzed with TEM under two different two beam diffraction conditions. When imaging under two beam conditions, the sample is tilted such that the incident beam satisfies the Bragg condition for one set of crystallographic planes. Any small deviation, such as a lattice distortion, from the Bragg condition will show up as a contrast in the image. Thus imaging under two beam conditions enhances strain contrast associated with this specific set of crystallographic planes. Shown in Fig. 2(a) is a TEM two beam image taken with $\vec{g}=[004]$ of a 100 nm $Sn_{0.06}Ge_{0.94}$/Ge(001) film in cross section. Contrast is observed near the surface but the remainder of the film is relatively featureless. In comparison, another cross sectional TEM image of the same sample taken with $\vec{g}=[1\bar{1}1]$ is shown in Fig. 2(b). Faint contrast in the shape of dark rods along [001] is discernable under these diffraction conditions. The dark rods do not penetrate the Ge substrate and are spaced approximately 17 nm apart. A high resolution TEM image of this $Sn_{0.06}Ge_{0.94}$/Ge(001) film, shown in Fig. 2(c), taken along the [110] zone axis has continuous lattice fringes at the film-substrate interface demonstrating that the $Sn_{0.06}Ge_{0.94}$ film adopts the Ge(001) substrate lattice parameter. Thus the contrast observed in Fig. 2(b) is not attributable to dislocations. In order to study the effect of film thickness on microstructure, a 1 μm thick $Sn_{0.03}Ge_{0.97}$/Ge(001) film was also imaged under two different two beam conditions to probe the strain state of this film. Cross sectional TEM images of the $Sn_{0.03}Ge_{0.97}$/Ge(001) film imaged under $\vec{g}=[004]$ and $\vec{g}=[\bar{2}20]$ two beam conditions are shown in Figs. 3(a) and 3(b), respectively. More contrast is observed when this same 1 μm thick film was imaged under $\vec{g}=[\bar{2}20]$ versus $\vec{g}=[004]$ two beam conditions. The periodicity of the dark regions was measured as approximately 65 nm. In distinction to the 100 nm thick $Sn_{0.06}Ge_{0.94}$/Ge(001) film, the dark rods oriented along [001] were still visible when the 1 μm thick $Sn_{0.03}Ge_{0.97}$ film was imaged under $\vec{g}=[004]$ two beam conditions.

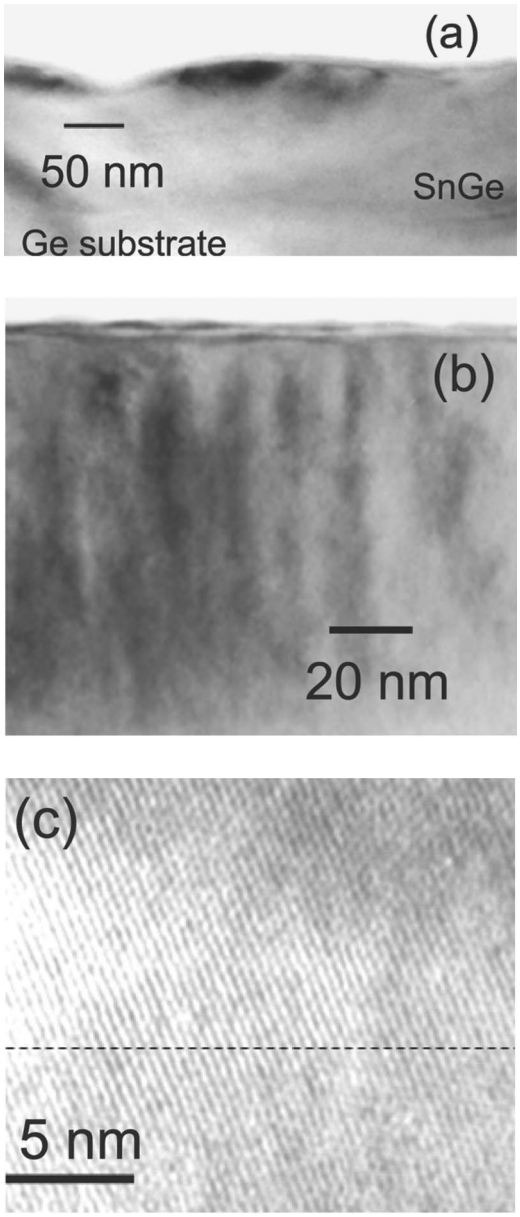

FIG. 2. $Sn_{0.06}Ge_{0.94}$/Ge(001) cross sectional TEM images under two beam conditions with (a) $\vec{g}=(004)$ (the $Sn_{0.06}Ge_{0.94}$ and Ge regions are labeled) and (b) $\vec{g}=[1\bar{1}1]$ (the $Sn_{0.06}Ge_{0.94}$/Ge(001) interface is at the bottom of the image). (c) HR-TEM image where the dashed line indicates the interface.

C. Z-contrast imaging

Contrast seen in conventional TEM mode is a combination of strain and composition. In order to decouple strain and composition, scanning transmission electron microscopy (STEM) with an annular detector was employed to measure contrast mainly due to composition.[11] The annular detector measures wide angle scattered electrons ($\alpha>80$ mrad). Diffracted intensity is attenuated at large angles; therefore, the intensity observed at large angles is primarily composed of

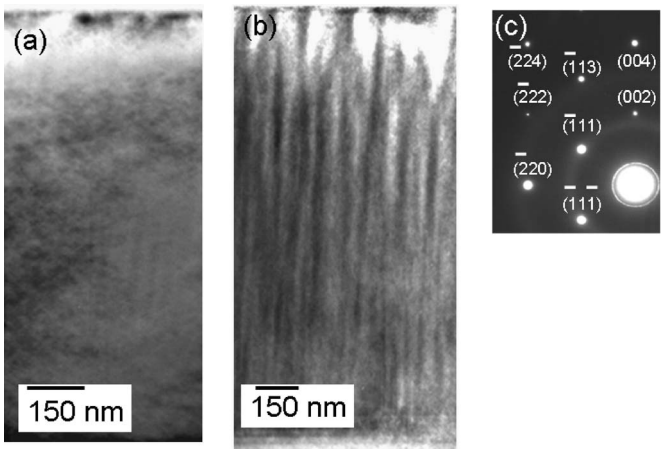

FIG. 3. Cross-sectional TEM images of 1 μm thick $Sn_{0.03}Ge_{0.97}/Ge(001)$ film imaged under (a) $\vec{g}=[004]$ and (b) $\vec{g}=[2\bar{2}0]$ two beam conditions. (c) A selected area diffraction pattern of the $Sn_{0.03}Ge_{0.97}/Ge(001)$ film demonstrating that the film is single crystalline.

elastically scattered electrons.[11] The elastic cross section depends on the atomic number, yielding composition contrast or *Z* contrast. The atomic number of Sn is 50 and that of Ge is 32; thus, measurable *Z* contrast is expected. The spot size of the electron beam in scanning mode was 5 nm.

Using the diffracted and transmitted beams, referred to as bright field imaging, a STEM image of the 100 nm thick $Sn_{0.06}Ge_{0.94}$ film prepared in planar view is shown in Fig. 4(a). The image does not have periodic features. In Fig. 4(b), the STEM image taken with the annular detector measuring elastically scattered electrons, referred to as dark field imaging, of the 100 nm thick $Sn_{0.06}Ge_{0.94}$ film is shown. Although slight variations in contrast are observable, the variations are not periodic and are on a larger length scale, $\approx 20x$, than observed in the TEM cross section of the same sample shown in Fig. 2(b). The lack of correlation between the contrast observed in cross-sectional TEM and STEM and between bright field and dark field STEM images is consistent with a homogeneous $Sn_{0.06}Ge_{0.94}/Ge(001)$ alloy. The small variation in contrast in the planar view image of this 100 nm thick film has a feature size on the order of 300 nm and is likely due to thickness variations across the STEM specimen. The results of the STEM analysis were quite different for the 1 μm thick $Sn_{0.03}Ge_{0.97}/Ge(001)$ film. Shown in Fig. 5(a) is a planar view STEM bright field image of this $Sn_{0.03}Ge_{0.97}/Ge(001)$ film. This image consisted of dark circular regions with the same 65 nm periodicity observed in cross-sectional TEM. Using the annular detector to measure elastically scattered electrons, the dark circular regions in the bright field STEM image of Fig. 5(a) appear as bright regions in the dark field image of Fig. 5(b). Due to the higher cross section for elastically scattered electrons (atomic number) of Sn versus Ge, the transition from dark to bright as the STEM conditions change from bright field to dark field imaging demonstrates that the circular regions are Sn rich. Thus, Sn is phase separating into wirelike features along the [001] growth direction in the 1 μm thick Sn_xGe_{1-x} films but not in the 100 nm thick film. Phase separation in these strained Sn_xGe_{1-x} films is consistent with linear instability models of alloy film growth. These models predict that surface roughening can relieve strain in epitaxial films without dislocation formation. The resultant roughened surface has preferred regions for Sn incorporation into the growing film. With rare exceptions, these models are not strictly sensitive to film thickness, but some exponential growth time is required before their predicted perturbations are experimentally observable, which is consistent with the observation of phase separation contrast in thick films, but not in thin ones. The origins of the experimentally observed contrast are discussed in Sec. III D. A pure material and two binary alloy linear instability models of heteroepitaxial film growth are discussed in Sec IV. A comparison of the model predictions with the experimental results is presented in Sec. V.

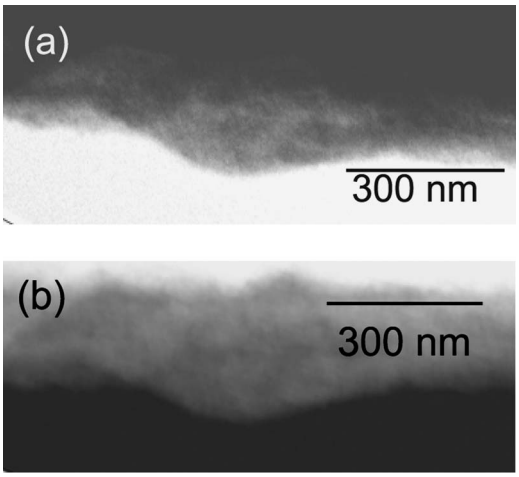

FIG. 4. STEM analysis of 100 nm thick $Sn_{0.06}Ge_{0.94}/Ge(001)$ film. (a) Bright field image includes diffracted and transmitted beams and (b) dark field image includes only elastically scattered electrons.

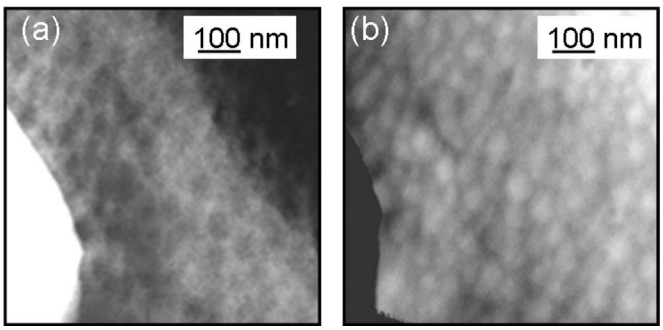

FIG. 5. STEM images of 1 μm thick $Sn_{0.03}Ge_{0.97}/Ge(001)$ (a) bright field image with transmitted and diffracted beams and (b) dark field image that includes only elastically scattered electrons.

D. Discussion

It is well known that a biaxially strained film, as is Sn_xGe_{1-x} on Ge(001), can undergo surface roughening during epitaxial growth to reduce elastic strain energy without forming misfit dislocations. A film under nonhydrostatic stress reduces strain energy by forming a surface undulation

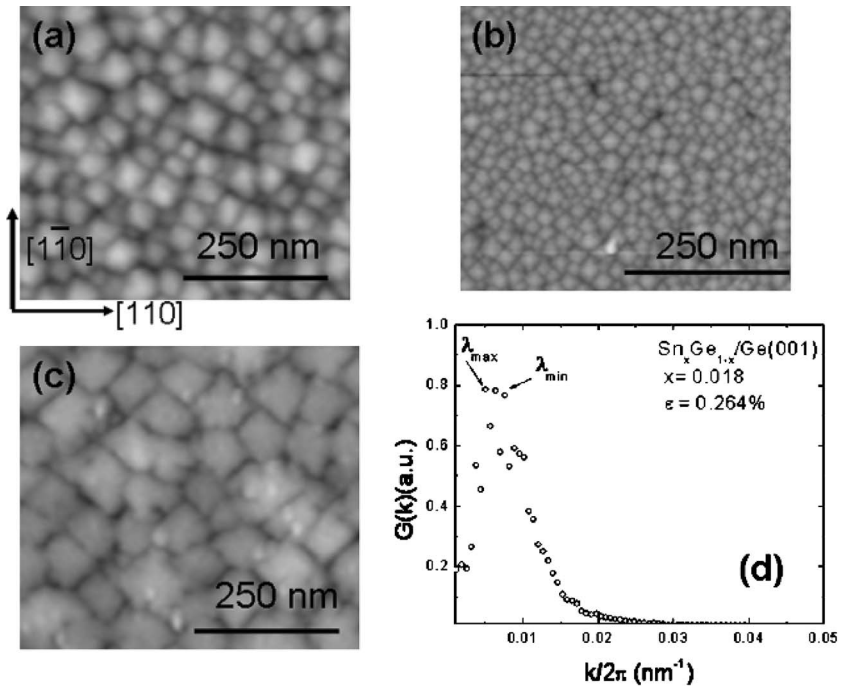

FIG. 6. Planar view AFM images of (a) $Sn_{0.018}Ge_{0.982}/Ge(001)$ with $\varepsilon=0.26\%$, (b) $Sn_{0.018}Ge_{0.982}/Si_yGe_{1-y}/Ge(001)$ with $\varepsilon=0.5\%$, and (c) $Ge/Si_yGe_{1-y}/Ge(001)$ with $\varepsilon=0.5\%$. (d) Power spectral density versus instability wave vector for $Sn_{0.018}Ge_{0.982}/Ge(001)$ with $\varepsilon=0.264\%$. The error in determining the peak value is represented as λ_{max} and λ_{min}, referring to the uncertainty in measuring the k vector associated with the peak value. The instability wavelength is 150 nm, 95 nm, and 224 nm in (a), (b), and (c), respectively.

where the lattice relaxes locally at the crest of the undulation. This phenomena is often referred to as an Asaro-Tiller-Grinfel'd (ATG) instability.[12,13] Biaxial strain has also been identified as a driving force for phase separation.[14,15] During epitaxial growth of Sn_xGe_{1-x} films under biaxial compression, the large Sn atoms may segregate via surface diffusion to the crest of a surface undulation that results from ATG instability. Surface diffusion of Sn to the crest will lead to the formation of Sn-enriched Sn_xGe_{1-x} nanowires oriented along [001] as the film thickness increases. The difference in contrast when imaging under two different two-beam conditions is in agreement with Sn phase separation via this kinetic mechanism as is the lack of evidence of phase separation in thinner films. The kinematical equation for the diffracted intensity, $|\Psi_g|^2$, under two beam conditions is shown.[16]

$$|\Psi_g|^2 = \frac{\Psi_0^2}{\xi_g}\int_{-t/2}^{t/2} e^{2\pi i(sz-\vec{g}\cdot\delta\vec{r})}dz, \qquad (1)$$

where $\delta\vec{r}$ is the lattice distortion, ζ_g is the extinction distance, s is the deviation parameter, t is the specimen thickness, and Ψ_o is the incident intensity. The strain contrast arises from the $\vec{g}\cdot\delta\vec{r}$ term in the exponent of Eq. (1). TEM contrast should be dominated by composition when $\vec{g}=[004]$ because $\delta\vec{r}$ and $\vec{g}$ are orthogonal. In the case of the 100 nm thick $Sn_{0.06}Ge_{0.94}/Ge(001)$ film, contrast is not evident when $\vec{g}=[004]$ and insignificant during STEM imaging of elastically scattered electrons. The contrast observed when $\vec{g}=[111]$ is thus likely associated with the formation of the surface undulation and strain rather than phase separation. In the case of the 1 μm thick $Sn_{0.03}Ge_{0.97}/Ge(001)$ film, if Sn segregates along (100) and (010) planes, the larger Sn atoms can coherently distort the lattice and $\delta\vec{r}=[100]$ and [010] and greater contrast is observed when $\vec{g}=[\bar{2}20]$ versus $\vec{g}=[004]$ two beam conditions. Similar contrast is seen in the textbook example of Guyer Preston (GP) zones in the Cu-Al system where Cu precipitates segregate along {001} planes. The Cu precipitates are visible in TEM when the diffracted beam is parallel with the lattice distortion.

IV. STATISTICAL ANALYSIS OF GROWTH INSTABILITY WAVELENGTH

A. Experimental determination

The period of the surface undulation observed in AFM and the periodicity of the phase separation, referred to previously as the growth instability wavelength, observed in TEM were correlated. The surface undulation as measured by AFM had feature heights measured to be on the order of 2 nm. The dependence of the instability wavelength on strain and Sn composition is evident in the AFM images of Fig. 6. The effect of strain independent of Sn composition can be seen by comparing a $Sn_xGe_{1-x}/Ge(001)$ and a $Sn_xGe_{1-x}/Si_yGe_{1-y}/Ge(001)$ film with the same Sn composition ($x=0.018$) but with different values of misfit. The AFM images of these films with misfit of 0.26% and with a misfit of 0.5% are shown in Figs. 6(a) and 6(b), respectively. The growth instability wavelength decreased from 155 to 95 nm with increasing misfit at this constant Sn composition of 1.8%. An AFM image of a $Ge/Si_yGe_{1-y}/Ge(001)$ film with a misfit of 0.5% is seen in Fig. 6(c). By comparing Figs. 6(b) and 6(c), increasing Sn composition from 0 to 1.8% at a fixed misfit of 0.5% decreased the instability wavelength from 224 to 95 nm. By comparing all of the images in Fig. 6, the instability wavelength is sensitive to composition independent of strain.

The growth instability wavelength was determined with greater precision by calculating the power spectral density (PSD) of the AFM images. The PSD, $G(k_x,k_y)$, was calculated from the surface topography by taking two-dimensional

(2D) Fourier transforms of the AFM images. In order to the improve statistics of the PSD, the directional dependence of the wave vector was discarded. Plots of PSD, $G(k)$, versus wave vector yielded a quantitative value for the fastest growing wave vector of the instability. The wave vector (k) of the instability is related to the instability wavelength (λ) by the following relationship: $k=2\pi/\lambda$. A typical spectrum of $G(k)$ versus k is displayed in Fig. 6(d) for the $Sn_{0.018}Ge_{0.982}/Ge(001)$ film shown in Fig. 6(a) having a misfit of 0.26%. The maximum corresponds to a wavelength of 155 nm. Statistical noise in the data blurs the peak of $G(k)$. The maximum and minimum value of the wavelength in Fig. 6(d) correspond to the error in determining the peak of $G(k)$.

B. Discussion

A surface that undergoes random deposition in the absence of atomic motion roughens equally at all wavelengths; hence, the PSD of a stochastic surface is constant versus wave number. Lateral smoothing mechanisms such as surface diffusion oppose the growth of a stochastic surface and lead to a decaying magnitude in the PSD with increasing wave number. Nonstochastic roughening processes can give rise to positive slopes in the PSD at small wave numbers. The combination of the positive slopes from nonstochastic roughening processes and the negative slopes from smoothening processes give rise to a peak in the PSD. According to linear response theory, in the presence of different roughening and smoothing mechanisms, the PSD will have the form[17]

$$G(k) \propto V \frac{\exp\left(2\sum_n C_n k^n t\right) - 1}{\sum_n C_n k^n}, \tag{2}$$

where the coefficients C_n are positive for roughening mechanisms and negative for smoothing mechanisms. At very early times or very small wave numbers, this reduces to $G(k) \propto \Sigma_n C_n k^n t$. At very late times or very large wave numbers, it reduces to $G(k) \propto (\Sigma_n C_n k^n)^{-1}$ (assuming the large wave number behavior is dominated by decaying modes). The slope of the log-log plot of the PSD versus the wave vector is the signature of the physical mechanism dominating surface smoothing (because they diverge exponentially with time, the surface roughening mechanisms are only identifiable as distinct positive slopes at very early times when the exponential can be linearized).

In order to determine if the low growth temperature was leading to a rough surface morphology, a strain free Ge/Ge(001) homoepitaxial film was grown at the Sn_xGe_{1-x} growth temperature, 433 K. The PSD for unstrained Ge at $T=433$ K, seen in Fig. 7(a), did not have a maximum and the decay of the signal at large k was proportional to k^{-2}, which is consistent with stochastic roughening smoothed by evaporation-condensation, as is expected for homoepitaxy. The temperature dependence of the growth instability wavelength is seen in the PSD of Fig. 7(b); strained Sn_xGe_{1-x} films were grown at $T=433$ K (closed squares) and 623 K (open squares) and show that the instability wavelength increases with increasing temperature. In Fig. 7(c), the instability wavelength is seen to decrease with increasing Sn composition and $G(k)$ decays as k^{-4}, which is generally considered indicative of smoothing by surface diffusion.

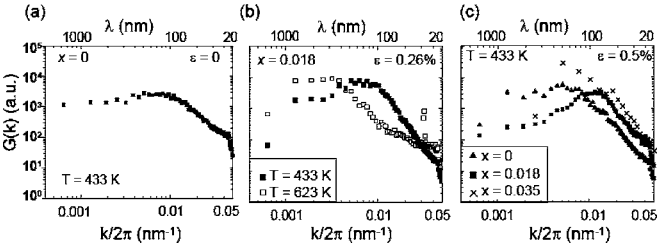

FIG. 7. Power spectral density versus wave vector for (a) unstrained Ge/Ge(001) film grown at $T=433$ K. (b) $Sn_xGe_{1-x}/Ge(001)$ with misfit of 0.26% grown $T=433$ K (closed squares) and $T=623$ K (open squares). (c) $Ge/Si_yGe_{1-y}/Ge(001)$ (closed triangles) and $Sn_xGe_{1-x}/Si_yGe_{1-y}/Ge(001)$ with $x=0.018$ (closed squares) and 0.035 (crosses). The misfit of the three films is 0.5%.

V. KINETIC MODEL VERSUS EXPERIMENT

Qualitatively in agreement with the ATG instability model, the observed instability wavelength decreases with increasing strain. Yet, the ATG instability model does not account for any change in the instability wavelength with changing alloy composition at constant misfit. Furthermore, the conditions of deposition are not considered by the ATG model at all. Since the phase separation of Sn into Sn_xGe_{1-x} wires is oriented along the growth direction, the instability was compared with two models[18,19] that incorporate mass transport mechanisms such as surface diffusion and incoming flux and which consider the properties of a binary alloy, A_xB_{1-x}. Lattice misfit with respect to the substrate and local composition fluctuations produce distinct strain fields in the alloy film and are separate driving forces for the growth instability. In addition, mass transport mechanisms, surface diffusion, and deposition are also factors shown by these models to lead to suppression or amplification of the growth instability.

A. Description of kinetic models

The detailed derivation of the models are given elsewhere,[12,13,15,18,19] so we focus on their governing equations and on the physical parameters needed to use these equations. Perturbations of the height and composition of the surface are characterized by linear stability analysis. Normal mode solutions of the form $\exp(\sigma t+\vec{k}\cdot\vec{x})$ are assumed, where σ is the amplification rate of the perturbation and $k=|\vec{k}|$ is its wave number. If $\mathrm{Re}(\sigma)<0$, then the system is stable; if $\mathrm{Re}(\sigma)>0$, then the system is unstable; and if $\mathrm{Im}(\sigma)\neq 0$, then an oscillatory instability is present.

1. Asaro-Tiller-Grinfel'd

In the study of stress-corrosion cracking, Asaro and Tiller[12] examined the competition between stress-driven

roughening and surface-energy-driven smoothing. They found that the dispersion relation between the amplification rate σ and the wave number k to be

$$\sigma = \frac{V_0^2 \Gamma_0 D^{\Sigma}}{RT} k^3 \left[\frac{2(1+\nu)E}{(1-\nu)} \varepsilon^2 - k\gamma \right]. \quad (3)$$

The stability of the interface is dominated at low k by elastic strain energy, in the form of $\sigma \propto \varepsilon^2 k^3$, and at high k by surface diffusion, in the form of $\sigma \propto -k^4$. The fastest growing wave number is $k_{\max,ATG} = (3/4)\varepsilon^2 2(1+\nu)E/[(1-\nu)\gamma]$. $V_0 = N_{Av} a^{f3}/8$ is the molar volume, $\Gamma_0 = 2/(N_{Av} a^{f2})$ is the molar surface density, R is the molar gas constant, N_{Av} is the Avogadro number, D^{Σ} is the intrinsic surface diffusivity, E is Young's modulus, ν is Poisson's ratio, ε is the applied strain, and γ is the surface energy. In the case of heteroepitaxy, $\varepsilon = (a^f - a^s)/a^s$ is the misfit strain between the film lattice parameter a^f and the substrate lattice parameter a^s. Grinfel'd[13] studied the mechanical equilibrium between elastic strain energy and surface energy, without consideration of kinetics, so there is no prediction of the fastest growing wave number, but his critical wave number (where perturbations neither grow nor decay) is identical to that of Asaro and Tiller.

2. Guyer-Voorhees

Unlike the static, uniform films described by the ATG model, technologically relevant films are deposited over a finite time and frequently contain two or more alloy components. Guyer and Voorhees[15,18] extended the ATG model to consider the effect of deposition as well as the thermodynamic stability and compositional strain of binary alloys. From the thermodynamics of stressed solids,[20] they determined the Gibbs-Thomson relation, relating the composition of the film surface to the surface curvature and stress state of the film. Surface diffusion is driven by gradients in this chemical potential, and they applied a network constraint (the diffusion of A atoms is matched by an equal and opposite flux of B atoms), which effectively says that the surface acts like a two-dimensional version of the bulk crystalline lattice. They assumed that deposition is governed by the Hertz-Knudsen condition, such that the deposition flux is perturbed by variations in the chemical potential along the surface. The combination of this local thermodynamic equilibrium condition with conditions of mechanical equilibrium throughout and mass balance at the film-vapor interface yield a dispersion relation:

$$\sigma^2 - \sigma\left\{ D^{\Sigma *} k^3 \left(\varepsilon^{*2} - \frac{k\gamma}{\chi} \right) + kV \left[(\varepsilon^* + \eta^*)^2 - \frac{k\gamma}{\chi} - 1 \right] \right\} - kV \left\{ D^{\Sigma *} k^3 \left[\varepsilon^{*2} + (\eta^{*2} - 1)\frac{k\gamma}{\chi} \right] + kV \left(\varepsilon^{*2} + \varepsilon^* \eta^* + \frac{k\gamma}{\chi} \right) \right\} = 0. \quad (4)$$

This equation is expressed in terms of a scaled misfit strain $\varepsilon^* = \{2(1+\nu)E/[\chi(1-\nu)]\}^{1/2}\varepsilon$, a scaled solute expansion coefficient $\eta^* = \{2(1+\nu)E/[\chi(1-\nu)]\}^{1/2}\eta\Delta\bar{x}$, an effective surface diffusivity $D^{\Sigma *} = V_0^2 \Gamma_0 D^{\Sigma}[G_v'' + 2\eta^2 E/(1-\nu)](1-x)x/RT$, and a chemical energy density $\chi = [G_v'' + 2\eta^2 E/(1-\nu)]\Delta\bar{x}^2$. In these terms, $G_v'' = \partial^2 G_v/\partial x^2$ where G_v is the Gibbs free energy per unit volume, $G_v'' = [RT/[x(1-x)] - 2\Omega]/V_0$ for a regular solution, Ω is the alloy interactioncoefficient, $\eta = (\partial a^f/\partial x)/a^f$ is the solute expansion coefficient that describes the dependence of the lattice parameter on composition, and $\Delta\bar{x} = 1 - x$.

This Guyer and Voorhees (GV) model has successfully described a number of experiments that cannot be explained by the ATG model. The model predicts that films grown under tension can be more stable than films grown under compression; this effect has been seen in both SiGe[9] and in InGaAs.[21] Sutter and Lagally[22] have found that the morphological instability wavelength scales as ε^{-1} for different compositions of SiGe deposited on Si. They find good agreement for this scaling using the GV model, as opposed to the ε^{-2} scaling of ATG. Finally, if $\eta^* > 1$, complex solutions to Eq. (4) are possible, even in the absence of misfit. As shown in Ref. 15, one possible consequence of complex values of σ are traveling waves where, in cross section, the composition modulations are at an angle to the growth direction. Peiró *et al.*[23] have found excellent agreement between the predictions of Ref. 15 and their MBE growth of InGaAs and InAlAs near-lattice-matched to vicinal InP.

In spite of the successful comparisons between experiments and the GV model, the underlying assumption of local equilibrium in the model is troublesome as a description of MBE growth. This artifice was used in order to establish the chemical potential, and hence the composition, at the surface of the growing crystal. This is not to suggest that the growing crystal is *in equilibrium* with an overlying vapor, but rather that there is "enough" exchange between the crystal surface and the atoms in the vacuum chamber, including the deposition beam, to define a chemical potential at the crystal surface. The local equilibrium assumption is successfully applied in a wide variety of nonequilibrium phase transformation processes, but generally between relatively dense phases of solid, liquid, or atmospheric gas. Even for "far from equilibrium" MBE, Seki, Koukitu, and co-workers have shown that equilibrium thermodynamic constants hold very well for the growth of III-V[24] and II-VI[25] alloys. The alloys in those papers have high vapor pressures and the effects of equilibrium were generally observed within about 100 K of the congruence temperature. In contrast, Sn and Ge have low vapor pressures, particularly at the low substrate temperatures studied in this paper (at 433 K, the equilibrium pressures of Sn and Ge are on the order of 10^{-28} Pa to 10^{-30} Pa (10^{-30} Torr to 10^{-32} Torr) despite the low melting point of Sn.[26] So, while local equilibrium may be a defensible assumption for some alloys grown near their congruence point, it is harder to justify for the low vapor pressure alloys considered here.

3. Spencer-Voorhees-Tersoff

Because the local equilibrium assumption in the GV model has been controversial as a description of MBE growth, Spencer, Voorhees, and Tersoff[19] have developed a similar model that removes this condition and further allows the two alloy species to diffuse independently, with different

surface mobilities. Much of their derivation is identical to the GV model, but by removing the assumptions of local equilibrium and the network constraint on surface fluxes, they obtain very different predictions. We will refer to their model as SVT. When Ge is taken to diffuse much faster than Si, Spencer *et al.* found excellent agreement between the most unstable wavelength and film composition for a number of different SiGe/Si experiments, including those of Ref. 22. Like the GV model, the SVT model predicts that tensile misfit can be more stable than compressive and that oscillatory or traveling waves are possible, but notably *only when the diffusivities of the alloy species are different*.

Although their assumption of different surface mobilities for different alloy species is certainly realistic, it is difficult enough to identify even one surface mobility for most semiconductor alloys and SnGe is no exception; we therefore consider the SVT model in the limit of identical mobilities (their case IV). We will discuss the qualitative effects of different mobilities in Sec. V C. Cast in the notation of the GV model, the SVT dispersion relation is

$$\sigma^2\left(1+\frac{k^2D^{\Sigma^*}}{V}\right)-\sigma\left\{\left(1+\frac{k^2D^{\Sigma^*}}{V}\right)D^{\Sigma^*}k^3\left(\varepsilon'^2-\frac{k\gamma}{\chi'}\right)+D^{\Sigma^*}(\eta'^2-1)k^3-kV\right\}-D^{\Sigma^*}k^3\left\{kV\left[\varepsilon'^2-\frac{k\gamma}{\chi'}\right]+D^{\Sigma^*}\left(\varepsilon'^2+(\eta'^2-1)\frac{k\gamma}{\chi'}\right)\right\}=0. \quad (5)$$

The terms are the same as in the GV model, with the exceptions of the new scalings $\varepsilon'=\{2(1+\nu)E/[\chi'(1-\nu)]\}^{1/2}\varepsilon$, $\eta'=\{2(1+\nu)E/[\chi'(1-\nu)]\}^{1/2}\eta\sqrt{x(1-x)}$, and $\chi'=[G_v''+2\eta^2E/(1-\nu)]x(1-x)$.

B. Comparison to experiment

Equations (3)–(5) were solved numerically for the Sn_xGe_{1-x} alloy system in order to calculate the value of the fastest growing instability wavelength predicted by the respective models and compare these to the measured experimental results. Although the quadratic dispersion relations (4) and (5) have two solutions, generally only one has experimentally observable positive values. The elastic constants were determined from the elastic stiffnesses as $E_{(100)}=(C_{11}+2C_{12})(C_{11}-C_{12})/(C_{11}+C_{12})=7.73\times10^{10}$ J/m^3 and $\nu_{(100)}=C_{12}/(C_{11}+C_{12})=0.286$ (Ref. 27). The stiffness is assumed independent of composition and taken to be the mean of the values for Ge:[28] $C_{11}=12.853\times10^{10}$ J/m^3, $C_{12}=4.826\times10^{10}$ J/m^3, $C_{44}=6.680\times10^{10}$ J/m^3, and for Sn:[28] $C_{11}=6.9\times10^{10}$ J/m^3, $C_{12}=2.93\times10^{10}$ J/m^3, $C_{44}=3.62\times10^{10}$ J/m^3. The interaction parameter $\Omega=27$ kJ/mol was determined by fitting the solidus curve on the Sn-Ge phase diagram.[29] The solute expansion coefficient is approximated as $\eta=(a^{Sn}-a^{Ge})/a^{Sn}=0.128$. The value of the surface diffusivity used in the calculation was $D^{\Sigma}=(8.45\times10^{-6}\ \text{cm}^2/\text{s})\exp(-0.83\ \text{eV}/kT)$[30] and corresponds to pure Ge. We compared two values of surface energy, $\gamma=1.927$ J/m^2 (Ref. 31) and $\gamma=0.85$ J/m^2 (Ref. 32). The first value corresponds to an unreconstructed Ge surface and the second is an estimate of how the surface energy is lowered by undergoing a 2×1 surface reconstruction.

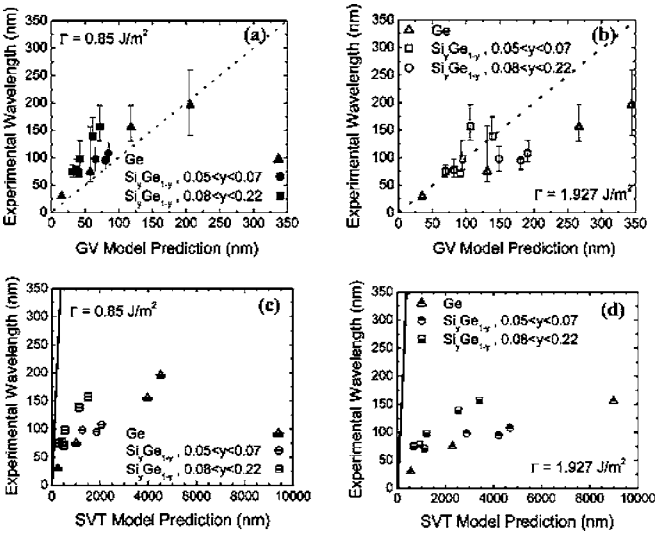

FIG. 8. Comparison of experimentally determined instability wavelength versus that predicted by (a) and (b) the GV model and (c) and (d) the ATG and SVT models. The surface energy is taken as (a) and (c) 0.85 J/m^2 and (b) and (d) 1.927 J/m^2. Triangles indicate Sn_xGe_{1-x} alloys grown on Ge(001) substrates, circles indicate alloys grown on Si_yGe_{1-y}/Ge(001) virtual substrates with $0<y<0.07$, and squares indicate alloys grown on Si_yGe_{1-y} virtual substrates with $0.07<y<0.22$. The line represents a one to one correlation. [Note: error bars were not plotted for (c) and (d) due to lack a of correlation between model and experiment.]

Figure 8 compares the experimental value of the fastest growing wavelength versus the GV model for (a) $\gamma=0.85$ J/m^2 and (b) $\gamma=1.927$ J/m^2 and versus the ATG and SVT models for (c) $\gamma=0.85$ J/m^2 and (d) $\gamma=1.927$ J/m^2 (note the change in horizontal axis). The line represents a one to one correlation and is included as a guide to the eye. Although all of the error bars do not cross the line, the agreement between the GV theory and experiment is reasonable (about a factor of 2 and sometimes within a few percent) considering the uncertainties in many of the parameters in Eq. (4). In contrast, the ATG model predicts wavelengths that are generally 10 to 40 times larger (never less than two times larger) than in the experiment. Given that ATG considers neither alloying strain nor deposition, it is unsurprising that it does not capture the behavior of Sn_xGe_{1-x} alloy film growth. What is more striking is that the SVT model, which is intuitively a better representation of MBE conditions than the local-equilibrium GV model, predicts behavior that is indistinguishable from ATG. This is because the SVT instability prediction reduces to the ATG instability prediction when the effective deposition rate is either very slow or very fast. At 433 K our deposition conditions are considered very fast and at 623 K they are considered very slow. Even allowing for a large uncertainty in the growth temperature (and hence in the effective deposition rate), with $\eta=12.8\%$ for Sn_xGe_{1-x}, there is no deposition rate for which the SVT wavelength from Eq. (5) is more than 20% smaller than the ATG wavelength (see, e.g., Fig. 4 of Ref. 19). To achieve a tenfold reduction in wavelength would require a three to five order of magnitude

decrease in the effective deposition rate *and* $\eta > 45\%$, neither of which is reasonable.

In each frame of Fig. 8, the Si composition range is shown as an inset in the figure. We notice that at the lower surface energy the virtual substrates with a lower Si content, $y < 0.07$ (shown as circles and triangles) have a better agreement with the GV model and similarly the virtual substrates with higher Si content, $y > 0.08$, (shown as squares) have greater agreement with the GV model prediction at higher surface energy. The surface energy of the film may change with Sn composition, an effect that is also not incorporated in the analysis. Pure Sn has a lower surface energy than Ge and if we invoke the virtual crystal approximation, we expect the surface energy of the Sn_xGe_{1-x} alloy to be lower than pure Ge. In Fig. 8(b), increasing surface energy indeed increases the value of the instability wavelength predicted by the kinetic model.

The fastest growing wavelength in the ATG model is proportional to the surface energy. The fastest growing wavelength in the SVT model is more weakly dependent on deposition rate than is the GV model, so its fastest growing wavelength is also essentially proportional to surface energy. Even if, despite the low deposition temperature, significant Sn segregation had occurred, the surface energy is unlikely to be 10 or 20 times smaller than the values we have assumed. Therefore, reasonable changes in the surface energy are able to bring the predictions of the GV model into agreement with experiment, but no reasonable changes to surface energy alone can produce agreement between experiment and the ATG or SVT models.

C. Discussion

Although the detailed predictions of any linear stability theory should not be taken too literally in the nonlinear regime observable in experiments, the PSD plots of Fig. 7(b) exhibit interesting differences in smoothing behavior between the low and high temperature films, which are consistent with the GV model. At low temperature, the amplitude decays at a slope somewhat greater than k^{-4}. In contrast, the high temperature film exhibits a decay in amplitude that scales as k^{-4}, but which has an abrupt inflection to k^{-1} at $k/2\pi \approx 0.01$ nm^{-1}. If we use the predictions of Eqs. (4) and (5) to plot Eq. (2), i.e., $G(k) \propto V[\exp(2\sigma t) - 1]/\sigma$, we obtain Fig. 9. The predictions of the GV model are in surprisingly good agreement with Fig. 7(b). All parameters used are obtained from the literature, as described above. The curves for the two temperatures have been normalized to give the same maximum value of $G(k)$, as is seen experimentally in Fig. 7(b). In Figs. 9(a)–9(c), the elapsed time is 2×10^4 s to give 1 μm total film thickness. In Fig. 9(b), the elapsed time has been increased to 10^5 s, in order to accentuate the elastically driven maximum. All of the models considered here employ normal mode analysis, with exponential amplification rates. As a result, the perturbations are only expected to be observable after elapsed times on the order of $1/\sigma$. The GV model predicts this elapsed time to be consistent with the observations. Because the magnitudes of σ predicted by the SVT model are much smaller than those predicted by the GV model, the elapsed time must be increased to a completely unrealistic 10^5 s in Fig. 9(d), in order to see the maximum at 623 K; at 433 K, over one hundred times longer is required before the maximum is observable. In contrast, the high k smoothing behavior is largely insensitive to elapsed time. Given that no nonlinear effects have been considered and no fitting parameters have been used, the degree of agreement between Figs. 7(b), 9(a), and 9(b) is extraordinary. While the power spectra for the GV model have the same axis ranges as the experimental plots in Fig. 7, the SVT power spectra are plotted over twice as many decades in the vertical axis and the wave number axes have been shifted down by an order of magnitude. As such, Figs. 9(a) and 9(b) are in much better agreement with Fig. 7(b) than are Figs. 9(c) and 9(d).

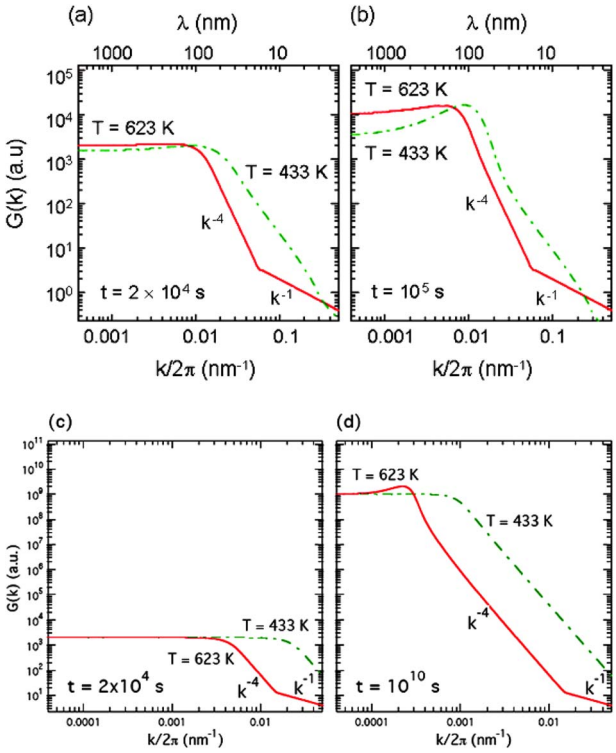

FIG. 9. (Color online) Simulated power spectra at two different deposition times. In both cases, $\gamma = 0.85$ J/m^2. Frames (a) and (b) are for the GV model, based on substitution of Eq. (3) into Eq. (2). Frames (c) and (d) are for the SVT model, based on substitution of Eq. (4) into Eq. (2). The elapsed time in (a) and (c) at the defined growth rate corresponds to a 1 μm film thickness. The elapsed times in (b) and (d) are chosen to emphasize the peak instability. Note the change in both vertical and horizontal axes between frames (a) and (b) and frames (c) and (d).

Of particular note is the inflection from k^{-4} to k^{-1} in the 623 K curves. The quadratic Eqs. (4) and (5) each have two solutions. In simple terms, one solution can be seen as approximately given by the ATG model, Eq. (3). The other solution is essentially $\sigma \propto -kV$. Because both the GV and SVT models consider deposition and stresses due to composition variations, both quadratic solutions deviate from these simple descriptions. The exact nature and magnitude of the deviations is dictated by the assumptions made in each model, but both models exhibit an "exchange of stability" at the intersection between the ATG-like solution and the mode

that is linear in k. In other words, if the first mode behaves like ATG at small waven umbers, then it will transition to $\sigma \propto -kV$ at large wave numbers. The other mode will transition from $\sigma \propto -kV$ at small wave numbers to the $\sigma \propto -k^4$ behavior of ATG at large wave numbers. The transition from $\sigma \propto -k^4$ to $\sigma \propto -kV$ gives rise to the transition from $G(K) \propto k^{-4}$ to $G(K) \propto k^{-1}$ in Fig. 9, and is consistent with the 623 K curve in Fig. 7(b). The GV and SVT models predict a similar wavelength for the transition. At 433 K, the transition is expected to occur at much large values of k, and it is indeed not observed in the range of the experimental data. We note that the region of the exchange has complex values for σ, but since they occur only over a narrow range of k and $\mathrm{Re}(\sigma) < 0$ for these experimental conditions, it is impossible to say what (if anything) would be observed in experiments. Unlike the conditions of Ref. 23, no macroscopically oscillatory or traveling behavior is expected.

It is important to note that we have neglected the possibility of different mobilities for the two alloy species, which is arguably the most important aspect of the SVT model. Although different species can certainly have different mobilities, the GV model is incapable of examining this effect because it assumes that surface diffusion obeys a "network constraint", where the flux of one alloy species is exactly balanced by an opposing flux of the other species. Analysis of the full SVT model with different mobilities for the different alloy components and with an arbitrary deposition rate is complicated, but when the effective deposition rate is high, the fastest growing wave number can be related to that of the ATG model as follows:

$$k_{\max,SVT} = k_{\max,ATG} \frac{1 + (\beta - 1)x\left[1 + (1 - x)\dfrac{\eta}{\varepsilon}\right]}{1 + (\beta - 1)x} \qquad (6)$$

and $\beta = D_{Sn}^{\Sigma}/D_{Ge}^{\Sigma}$. In order to bring $k_{\max,SVT}$ into agreement with the experimentally observed wavelengths, β ranges between 6 and 87 for $\gamma = 0.85\ \mathrm{J/m^2}$. If $\gamma = 1.927\ \mathrm{J/m^2}$, β can exceed 300; in some cases there is no value that brings the model into agreement with experiment. Equation (6) should be valid at 433 K, but not at 623 K, where the effective deposition rate is low; at the higher temperature, $\beta \approx 100$ would bring the full SVT model into agreement with experiment.[33] While these magnitudes of β are not impossible (and indicate that Sn diffuses faster than Ge, which is expected given their respective melting points), we find that a 1.5% Sn film can have $\beta = 17$, $\beta = 28$, or $\beta = 87$, solely as a function of substrate misfit. Although strain probably affects diffusivity, and may do so differently for different species, we cannot say whether the strain dependence predicted here is reasonable.

VI. CONCLUSION

We have grown 1 μm thick $Sn_xGe_{1-x}/Ge(001)$ and $Sn_xGe_{1-x}/Si_yGe_{1-y}/Ge(001)$ epitaxial films with $0 < x < 0.07$ that evolved during growth into a dense array of Sn-enriched Sn_xGe_{1-x} nanowires oriented along [001]. We compared the microstructure of 1 μm thick films to 100 nm thick films. In cross-sectional TEM images with two beam diffraction conditions having $\vec{g} = [004]$ and STEM analysis, phase separation was not observed in 100 nm thick films but strain was observed under two beam diffraction conditions with $\vec{g} = [1\bar{1}1]$ in these films and this strain was identified as a possible driving force for phase separation. In the case of the 1 μm thick films, the measured period of the phase separation in TEM was dependent on the Sn composition. The period of the phase separation was measured in cross-section TEM as 65 nm and the size of the Sn-rich regions was 23 nm for a Sn composition of $x = 0.03$. STEM Z-contrast analysis in planar view revealed a composition contrast consistent with Sn-rich Sn_xGe_{1-x} nanowires embedded in a Ge-rich matrix.

The phase-separation observed in STEM was correlated with a surface undulation that was measured in AFM. The PSD of the AFM images was calculated to experimentally measure the fastest growing wavelength of the growth instability. The experimental value was then compared to three models of heteroepitaxial film growth. The value of the instability wavelength predicted by the alloy models was more sensitive to strain than to composition. Experimentally, the composition had a greater impact on the instability wavelength. Nonetheless, the values for the instability wavelength predicted by the GV binary alloy film growth model are in reasonable agreement with the experimentally measured values. Most significantly, the GV model predicts a smoothing behavior as a function of temperature that correlates quite accurately with the experimental data. In contrast, the ATG model and the equal-mobilities case of the SVT model predict wavelengths more than an order of magnitude larger than observed. The failure of the pure-material, static film ATG model to predict the behavior of growing alloy films is unsurprising. More notable is the fact that the SVT model, developed to correct questionable assumptions in the GV model, makes predictions that are indistinguishable from the ATG model when the alloy component mobilities are assumed identical. If the different mobilities of Sn and Ge are considered, better agreement between SVT and the experimental data can be obtained by using the ratio of the mobilities as a fitting parameter, particularly if the mobilities of Sn and Ge are allowed to have different dependencies on misfit strain. In summary, comparison of experimental data with different instability models has led to greater physical insight in the mechanisms governing phase separation in a biaxially strained binary alloy.

ACKNOWLEDGMENTS

We would like to thank C.A. Ahn for help with electron microscopy. We thank W. Tong and P. W. Voorhees for discussions regarding analysis of the models, and are particularly grateful to B. J. Spencer for checking our use of the SVT model. We thank A. Polman's group at AMOLF in the Netherlands for the use of their accelerator for RBS analysis. R.R. acknowledges Intel as well as the University of California, Irvine for startup funds while the theoretical work was performed.

*Corresponding author. Present address: University of California, Irvine, Chemical Engineering and Materials Science, Irvine, California 92697-2575. Electronic address: rragan@uci.edu

[1] L. D. Hicks and M. S. Dresselhaus, Phys. Rev. B **47**, 16631 (1993).
[2] L. D. Hicks, T. C. Harman, and M. S. Dresselhaus, Appl. Phys. Lett. **63**, 3230 (1993).
[3] R. Ragan, C. C. Ahn, and H. A. Atwater, Appl. Phys. Lett. **82**, 3439 (2003).
[4] H. Zheng, J. Wang, S. E. Lofland, Z. Ma, L. Mohaddes-Ardabili, T. Zhao, L. Salamanca-Riba, S. R. Shinde, S. B. Ogale, F. Bai, D. Viehland, Y. Jia, D. G. Schlom, M. Wuttig, A. Roytburd, and R. Ramesh, Science **303**, 661 (2004).
[5] G. He and H. A. Atwater, Phys. Rev. Lett. **79**, 1937 (1997).
[6] R. Ragan and H. A. Atwater, Appl. Phys. Lett. **77**, 3418 (2000).
[7] R. Ragan and H. A. Atwater, Appl. Phys. A **80**, 1335 (2005).
[8] E. A. Fitzgerald, Y. H. Xie, M. L. Green, D. Brasen, A. R. Kortan, J. Michel, Y. J. Mii, and B. E. Weir, Appl. Phys. Lett. **59**, 811 (1991).
[9] Y. H. Xie, G. H. Gilmer, C. Roland, P. J. Silverman, S. K. Buratto, J. Y. Cheng, E. A. Fitzgerald, A. R. Kortan, S. Schuppler, M. A. Marcus, and P. H. Citrin,Phys. Rev. Lett. **73**, 3006 (1994).
[10] W. Wegscheider, J. Olajos, U. Menczigar, W. Dondl, and G. Abstreiter, J. Cryst. Growth **123**, 75 (1992).
[11] S. J. Pennycook, S. D. Berger, and R. J. Culbertson, J. Microsc. **144**, 229 (1986).
[12] R. J. Asaro and W. A. Tiller, Metall. Trans. **3**, 1789 (1972).
[13] M. A. Grinfel'd, Sov. Phys. Dokl. **290**, 1358 (1986).
[14] F. Glas, Appl. Surf. Sci. **123**, 298 (1998).
[15] J. E. Guyer and P. W. Voorhees, J. Cryst. Growth **187**, 150 (1998).
[16] B. J. Fultz and J. Howe, *Transmission Electron Microscopy and Diffractometry of Materials* (Springer, Pasadena, 2000).
[17] W. M. Tong and R. S. Williams, Ann. Rev. Phys. Chem. **45**, 401 (1994).
[18] J. E. Guyer and P. W. Voorhees, Phys. Rev. B **54**, 11710 (1996).
[19] B. J. Spencer, P. W. Voorhees, and J. Tersoff, Phys. Rev. B **64**, 235318 (2001).
[20] F. C. Larche and J. W. Cahn, Acta Metall. **33**, 331 (1985).
[21] J. E. Guyer, S. A. Barnett, and P. W. Voorhees, J. Cryst. Growth **217**, 1 (2000).
[22] P. Sutter and M. G. Lagally, Phys. Rev. Lett. **84**, 4637 (2000).
[23] F. Peiró, J. C. Ferrer, A. Cornet, M. Calamioutou, and A. Georgalkilas, Phys. Status Solidi A **195**, 32 (2003).
[24] H. Seki and A. Koukitu, J. Cryst. Growth **78**, 342 (1986).
[25] A. Koukitu, H. Nakai, T. Suzuki, and H. Seki, J. Cryst. Growth **84**, 425 (1987).
[26] R. E. Honig, RCA Rev. **23**, 567 (1962).
[27] L. D. Landau and E. M. Lifshitz, *Theory of Elasticity* (Pergamon Press, London, 1959).
[28] E. A. Fitzgerald, P. E. Freeland, M. T. Asom, W. P. Lowe, R. A. Macharrie, B. E. Weir, A. R. Kortan, F. A. Thiel, Y. H. Xie, A. M. Sergent, S. L. Cooper, G. A. Thomas, and L. C. Kimmerling, J. Electron. Mater. **20**, 489 (1991).
[29] N. Choly, Undergraduate Thesis, California Institute of Technology, 1999.
[30] E. Chason, J. Y. Tsao, K. M. Horn, S. T. Picraux, and H. A. Atwater, J. Vac. Sci. Technol. A **8**, 2507 (1990).
[31] J. M. Blakely, *Introduction to the Properties of Crystal Surfaces* (Pergammon Press, Oxford, 1973) Vol. 12.
[32] *Properties of Silicon Germanium*, edited by E. Kasper (INSPEC, London, 1995).
[33] B. J. Spencer (private communication).